The effect of melt-homogenization and heat-treatment on the optical properties of the rare earth doped oxyfluoride glass-ceramics

Li, Zhencai; Tan, L.L.; Chen, C.Y.; Zhou, D.C.; Jensen, Lars Rosgaard; Ren, J.J.; Zhang, Y.F.; Qiu, J.B.; Yue, Yuanzheng

Published in:
Journal of Non-Crystalline Solids

DOI (link to publication from Publisher):
10.1016/j.jnoncrysol.2022.121773

Publication date:
2022

Document Version
Publisher's PDF, also known as Version of record

Journal of Non-Crystalline Solids 593 (2022) 121773

Contents lists available at ScienceDirect

Journal of Non-Crystalline Solids

journal homepage: www.elsevier.com/locate/jnoncrysol

The effect of melt-homogenization and heat-treatment on the optical properties of the rare earth doped oxyfluoride glass-ceramics

Zhencai Li [a], Linling Tan [b], Chunying Chen [c], Dacheng Zhou [d], Lars R. Jensen [e], Jinjun Ren [c], Yanfei Zhang [f,*], Jianbei Qiu [d,*], Yuanzheng Yue [a,*]

[a] Department of Chemistry and Bioscience, Aalborg University, 9220 Aalborg, Denmark
[b] Laboratory of IR Materials and Devices, Ningbo University, Ningbo 315211, China
[c] Shanghai Institute of Optics and Fine Mechanics, Chinese Academy of Sciences, Shanghai, 201800, China
[d] School of Material Science and Engineering, Kunming University of Science and Technology, Kunming 650093, China
[e] Department of Materials and Production, Aalborg University, 9220 Aalborg, Denmark
[f] School of Materials Science and Engineering, Qilu University of Technology (Shandong Academy of Sciences), Jinan 250353, China

ARTICLE INFO

Keywords:
Glass-ceramics
Rare earth ions
Melt-homogenization temperature
Heat-treatment
Up-conversion luminescence
Light transmittance

ABSTRACT

We prepared four Er^{3+}-Yb^{3+} co-doped oxyfluoride precursor glass (PG) samples with the same chemical composition at different melt-homogenization temperatures (T_{homo}), respectively, at the same melt-quenching rate. We investigated the effect of T_{homo} and heat-treatment (HT) on the crystallization, structure, and optical properties of the four samples. The results show that the structural heterogeneity in the PG sample increases with lowering T_{homo}, and this promotes phase-separation, and hence, formation of Ba_2LaF_7 crystals. Consequently, the light transmittance of PG samples is decreased, but the up-conversion (UC) luminescence is enhanced. Moreover, the crystallinity of the four PG samples was increased by HT, and this altered the light transmittance, and greatly enhanced the UC luminescence. The mechanism of these discovered phenomena was discussed in terms of structure and crystal evolution. This work provides an effective way to optimize the optical and photonic performances of the rare earth doped oxyfluoride glass-ceramics.

1. Introduction

An oxyfluoride glass-ceramic (GC) is composed of both glass phase and fluoride crystals, and is produced by heat-treating its parent or precursor glass (PG) [1]. The PG is obtained by quenching its liquid state at a sufficient rate to bypass crystallization [2]. It was reported that the phase separation, e.g., the separation between the fluoride-rich and the aluminosilicate-rich phases in oxyfluoride glasses, could induce the formation of nanocrystals [3,4]. In other words, the fluoride crystals can be precipitated from the fluoride-rich phases in the PG via appropriate heat-treatment (HT). However, the growth of fluoride crystals in some oxyfluoride glasses is limited by the energy barrier for ionic diffusion in the liquid around crystals, and hence large crystals cannot be obtained [5–7]. It was reported that the small-sized fluoride crystals are difficult to accommodate more rare earth (RE) ions for optimizing optical properties for applications [1]. To achieve large-sized fluoride crystals in oxyfluoride glasses, some of the present authors recently designed numerous compositions, from which large fluoride crystals can be generated even during melt-quenching [8]. The thus-derived oxyfluoride glasses contained different kinds of fluoride crystals, such as $NaLuF_4$, KTb_2F_7, and K_3YF_6 [9–11].

Compared with traditional oxyfluoride glass-ceramics (GCs), the melt-quenching derived oxyfluoride GCs have the following two advantages. First, the latter ones contain larger fluoride crystals with low phonon energy, which can accommodate more RE ions, and this gives superior optical performances [12]. Second, the preparation of such new types of GCs is simpler and more energy-saving since the HT procedure for traditional GCs can be skipped [13]. Thus, the melt-quenching derived GCs have potential to be used as high-performance optical materials. However, the origin of the formation of the fluoride crystals in the oxyfluoride glasses still needs to be further investigated. In particular, revealing the relations between structural heterogeneity, crystal formation and functionalities in glass is a key for designing new types of functional glass-ceramics [14–16]. In this work, we investigated the impact of structural heterogeneity and phase separation on fluoride crystal formation and optical properties by varying the

* Corresponding authors.
E-mail addresses: zhang-yanfei@hotmail.com (Y. Zhang), qiu@kmust.edu.cn (J. Qiu), yy@bio.aau.dk (Y. Yue).

https://doi.org/10.1016/j.jnoncrysol.2022.121773
Received 4 May 2022; Received in revised form 16 June 2022; Accepted 26 June 2022
Available online 6 July 2022

melt-homogenization temperature (T_{homo}). We prepared the Er^{3+}-Yb^{3+} co-doped Ba_2LaF_7 melt-quenching derived oxyfluoride PG and GC samples by quenching the glass melt from four different T_{homo}. To study the structural and morphological evolution of the PG and GC samples during crystallization, we utilized X-ray diffraction, Raman spectroscopy and scanning electron microscopy on both the melt-quenched and the heat-treated samples. In addition, we detected the phase transition of the studied samples using differential scanning calorimetry. We determined the optical properties of the studied materials and identified the optimum T_{homo} for fabricating oxyfluoride GCs with high optical performances.

2. Experimental

The oxyfluoride PG and GCs with the molar composition of $45SiO_2$–$15Al_2O_3$–$12Na_2O$-$21BaF_2$–$7LaF_3$–$0.5ErF_3$–$1.0YbF_3$ were prepared by the melt-quenching method. 10 g raw materials, each component of which has a purity of 99.99%, were mixed and put into an alumina crucible with a lid, and then melted and homogenized in a box-type furnace in air atmosphere at 1450, 1500, 1550, and 1590 °C, respectively, for 45 min. Each melt was cast quickly onto a stainless-steel plate preheated at 300 °C. Subsequently, the obtained samples were annealed at 500 °C for 8 hours in a muffle furnace to release thermal stress and then cooled down to room temperature in the furnace. The above-derived samples were denominated as PG-1, PG-2, PG-3 and PG-4, according to the melt-homogenization temperatures of 1450, 1500, 1550, and 1590 °C, respectively. The four PG samples (PG-1, PG-2, PG-3, and PG-4) were subjected to heat-treatment (HT) at around $1.07T_{c1}$for 2 hrs. where T_{c1} is the onset temperature of the first crystallization (Fig. 1), and accordingly the heat-treated samples were named HT-PG-1, HT-PG-2, HT-PG-3 and HT-PG-4.

The studied samples were upscanned using differential scanning calorimetry (DSC, NETZSCH STA 449F3 Jupiter) at 10 °C/min in nitrogen atmosphere. X-ray diffraction (XRD) measurements were performed to identify the crystalline phase by a powder diffractometer operated at 45 KV and 40 mA, using Cu-Kα as the radiation. The Raman spectra in the range of 175–1200 cm^{-1} were obtained using a micro-Raman spectrometer (inVia, Renishaw) with a 532 nm green HeNe laser at room temperature. The microstructure of the samples was characterized by field-emission scanning electron microscopy (SEM, QUANTA 200) using a voltage of 30 kV. The chemical compositions of the samples were determined by the special aberration-corrected transmission electron microscope (ACTEM, FEI Titan Cubed Themis G2 300) equipped with High-Angle Annular Dark Field transmission electron microscope (HAADF-STEM) and selected area electron diffraction (SAED) at the voltage of 200 KV. The optical absorption spectra in the wavelength range of 275 to 1000 nm were acquired using a Varian Cary 50 spectrophotometer. The local structure in PG sample was characterized by performing the solid-state nuclear magnetic resonance (NMR) experiments (Bruker Avance III HD 500 MHz spectrometer (11.7 T)) at 25 °C. ^{27}Al magic angle spinning (MAS) NMR spectra were obtained at the resonance frequency of 130.2 MHz, operating with a 4 mm MAS probe at a spinning rate of 12 kHz. The typical pulse length was 0.83 μs (10° liquid flip angle). The relaxation delay was 0.5 s for all the samples. The chemical shifts of ^{27}Al were referenced to $Al(NO_3)_3$ (1 M) aqueous solution. The UC luminescence spectra were recorded in the wavelength range from 500 to 700 nm using a HITACHI F-7000 fluorescence spectrophotometer under the 980 nm laser excitation.

3. Results and discussions

3.1. Calorimetric analysis

Fig. 1a and b show the DSC curves of both PG (PG-1, PG-2, PG-3, and PG-4) and the heat-treated PG (HT-PG-1, HT-PG-2, HT-PG-3, and HT-PG-4) samples, respectively, from which the glass transition temperature (T_g), the first and second onset temperatures of crystallization peaks (T_{c1} and T_{c2}) and the first and second melting peaks (T_{p1} and T_{p2}) were determined (Table 1). It is seen that both T_g and T_{c1} slightly decrease with increasing melt-homogenization temperature (T_{homo}) for the PG samples prepared with temperatures up to 1550 °C. By further raising T_{homo} to 1590 °C, an increase of T_g and T_{c1} is observed. The T_g decrease could be attributed to the depolymerization of the glass network since the fluoride crystallites break down at T_{homo} = 1550 °C and hence, the fluorine ions as modifiers dissociate the network. In contrast, the T_g increase could be ascribed to the increase of the network

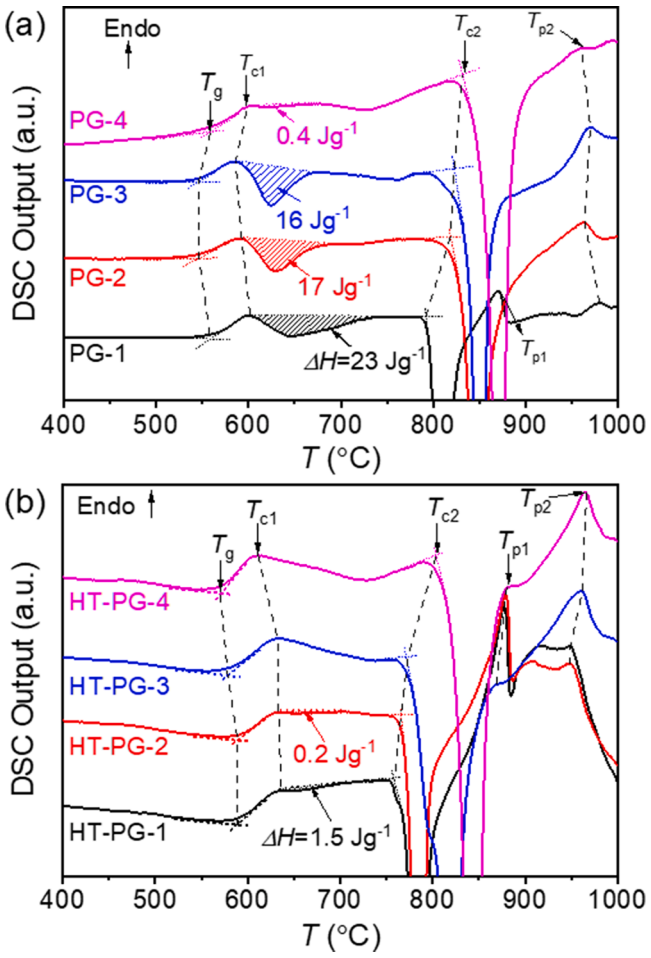

Fig. 1. Differential scanning calorimetry (DSC) output (arbitrary unit) of both PG samples (PG-1, PG-2, PG-3, and PG-4) **(a)** and the heat-treated ones (HT-PG-1, HT-PG-2, HT-PG-3 and HT-PG-4) **(b)**. T_g: the glass transition temperature; T_{c1} and T_{c2}: the onset temperatures of the first and second crystallization peaks, respectively; T_{p1} and T_{p2}: the temperatures of the first and second melting peaks, respectively. Hatched area: the crystallization enthalpies (ΔH) for the first exothermic peak.

Table 1
The onset temperatures (in °C) of the glass transition (T_g), the first and the second crystallization peaks (T_{c1} and T_{c2}), and the first and the second melting peaks (T_{p1} and T_{p2}) of both PG and the heat-treated PG samples, respectively.

Samples	T_g	T_{c1}	T_{c2}	T_{p1}	T_{p2}
PG-1	559	601	793	872	981
PG-2	547	593	819	~	965
PG-3	546	587	824	~	970
PG-4	558	600	831	~	961
HT-PG-1	591	637	758	877	950
HT-PG-2	590	635	765	879	951
HT-PG-3	578	633	772	870	963
HT-PG-4	571	612	803	881	967

polymerization degree as fluorides (SiF_4 and NaF_4) escape from the melts at higher T_{homo} (1590 °C) and thus the number of bridging oxygens increases [17]. In Fig. 1a, it is observed that T_{c2} of PG samples increases with increasing T_{homo}, indicating that the secondary crystallization needs higher temperature (i.e., higher kinetic energy) to be initiated. Increasing T_{homo} can help destroy some relatively ordered domains, that is, reduce the dynamical and structural heterogeneity in the melt, and thus increasing the energy barriers for nucleation to occur. This indicated that varying T_{homo} is an effective way to alter the crystallization behavior of glasses. It should be noted that the first melting peak for PG-2, PG-3, and PG-4 samples might be hidden in the second crystallization peak (see T_{p1}), whereas the melting peak is observable in the curve of PG-1 sample. In contrast, T_{p2} exhibits only a slight change with varying T_{homo}, meaning that the melting event is almost independent of the melt- homogenization history.

As shown in Fig. 1(b), both T_g and T_{c1} of the heat-treated PG samples are higher than those of the corresponding PG samples. This is attributed to the fact that the fraction of the connected [SiO_4] and [AlO_4] tetrahedral units in the glass matrix increases upon heat-treatment (HT) owing to the precipitation of the Ba_2LaF_7 crystals. Thus, the network connectivity of the glass phase increases, thereby making both T_g and T_{c1} higher [18]. The heat-treated PG samples exhibit lower T_{c2} than the PG samples, implying that the second crystallization occurs more easily. Comparing the DSC curves of both PG-1 (Fig. 1a) and HT-PG-1 (Fig. 1b), it is seen that the first melting peak in PG-1 becomes stronger due to the further formation of Ba_2LaF_7 crystals upon HT. In addition, the first melting peaks of HT-PG-2, -3 and -4 samples appear during DSC upscans, indicating that Ba_2LaF_7 crystals are precipitated from the glass matrix upon HT. The crystal precipitation is also confirmed by the XRD results (Fig. 3b). Thus, T_{p1} of the studied samples is the onset temperature of the melting of Ba_2LaF_7 crystals. Furthermore, each T_{p2} value of the heat-treated samples is lower than that of the PG samples [19].

To study the first crystallization behavior of both PG and the heat-treated PG samples, the crystallization enthalpies (ΔH) are obtained by calculating the area of the first exothermic peak as shown in Fig. 1(a and b). The ΔH of PG samples decreases with increasing T_{homo} (Fig. 1a), implying that the glass stability preventing the first crystallization event increases. This suggests that the degree of structural heterogeneity decreases with increasing T_{homo} [20]. It is seen in Fig. 1b that the HT makes the first crystallization peaks much smaller for samples HT-PG-1 and -2, and even disappeared for the samples HT-PG-3 and -4. This means that the formation of Ba_2LaF_7 crystals is already completed in the samples with higher T_{homo} (i.e., in HT-PG-3 and -4) during isothermal HT, and hence, the first crystallization peak does not exist during the subsequent DSC upscans. In contrast, the formation of Ba_2LaF_7 crystals is not completed in the samples with lower T_{homo} (i.e., in HT-PG-1 and -2) during HT, and thus, the first crystallization peaks appear during the DSC upscans despite they are tiny. In other words, the heat-treated PG samples exhibit higher crystallinity than the original PG samples.

To observe the crystallization event in PG samples, each sample was upscanned to 740, 700, 720, and 690 °C (above T_{c1}), respectively, three times at 10 °C/min equal to the subsequent cooling rate. The determination of T_g is shown in Fig. 2a-d, and the T_g values obtained from the first upscans are given in Table 1. It is seen that the first DSC upscan gives a lower T_g value than the second and third upscans, whereas the latter two upscans exhibit almost the same T_g. In addition, the area (i.e., enthalpy) of the first crystallization peak decreases with the number of DSC cycles and then remains nearly constant. This could be explained by the increased stability of the glass matrix after the crystal precipitation during the first upscan to T_{max}. In other words, during the dynamic heating process, a large portion of F^-, La^{3+}, and Ba^{2+} ions are depleted from the glass matrix and then migrate to the existing Ba_2LaF_7 crystals

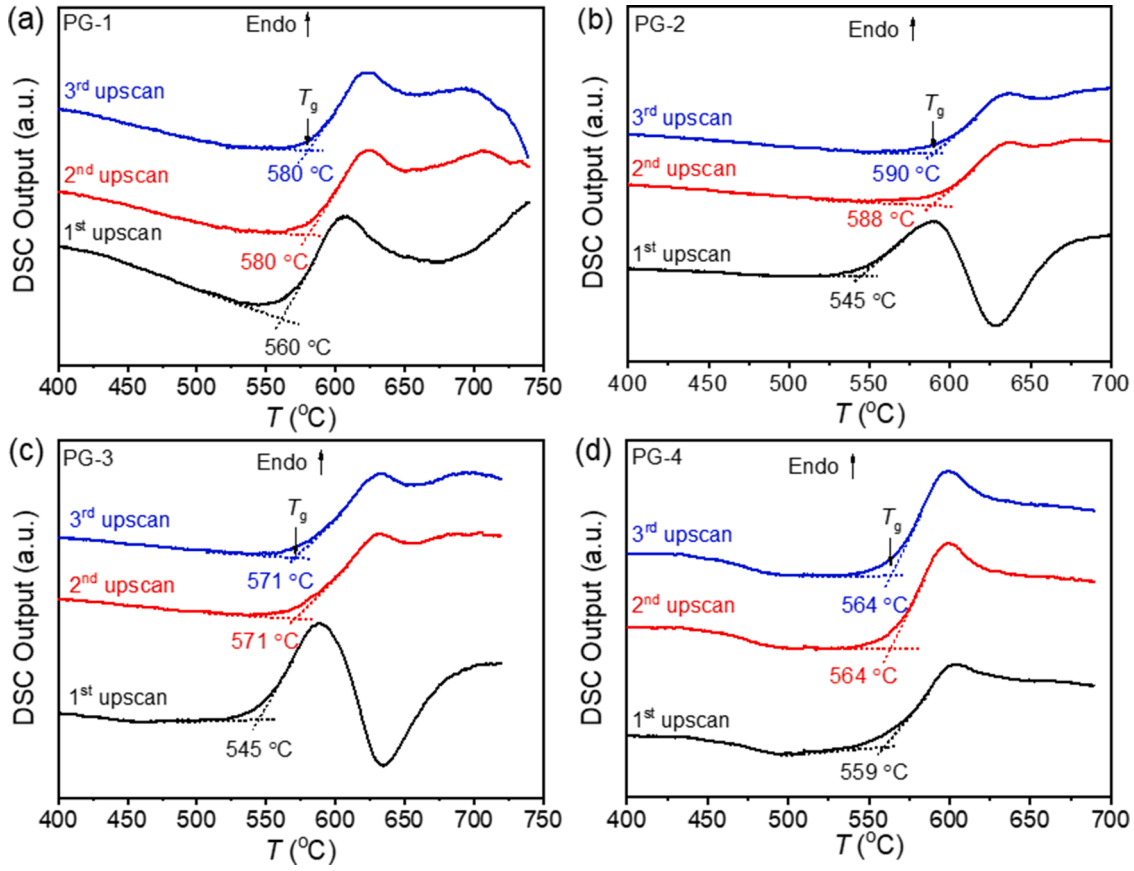

Fig. 2. DSC output (arbitrary unit) of PG-1 **(a)**, PG-2 **(b)**, PG-3 **(c)** and PG-4 **(d)** samples by repeated scans to maximum scanning temperatures of 740, 700, 720, 690 °C, respectively, for three times at the heating and cooling rate of 10 °C/min.

for further growth and also to the structural domains where nucleation can easily occur [21]. However, during the 2nd and 3rd upscans, the remaining glass matrix will not crystallize since both thermodynamic and kinetic barriers for nucleation are quite large owing to the high network connectivity.

3.2. Structural analysis

Fig. 3a shows the XRD patterns of the four PG samples, where diffraction peaks are detected in PG-1, -2 and -3 samples, and become weaker with increasing T_{homo}. These peaks are attributed to the face-centered cubic (FCC) Ba_2LaF_7 crystal (PDF#48–0099) [9]. However, two weak broad humps appear for PG-4 sample, implying its glassy nature [3,22]. This suggests that the formation of Ba_2LaF_7 crystals can be suppressed since the structural heterogeneity in the glass melt is drastically reduced by increasing T_{homo}. Upon isothermal HT, the diffraction peaks of samples HT-PG-1, -2 and -3 become stronger. Interestingly, several weak peaks are observed for sample HT-PG-4, and they are ascribed to Ba_2LaF_7 crystals, indicating that HT leads to an increase of Ba_2LaF_7 content in PG samples [23].

Fig. 4a and b show the Raman spectra of both PG and the heat-treated PG samples, respectively, which are normalized by the intensity of the peak at around 549 cm^{-1}. It is seen in Fig. 4a that the Raman peak at 269 cm^{-1} becomes weaker and even disappears with increasing T_{homo} from 1450 to 1590 °C, i.e., for samples PG-1, -2, -3 and -4. The peak at 269 cm^{-1} is ascribed to the stretching mode of Ba-F and La-F bonds in Ba_2LaF_7 crystals, confirming the existence of Ba_2LaF_7 crystals in PG-1, -2 and -3 samples. The Raman peaks in the wavelength range of 388-691 cm^{-1} are assigned to symmetric stretching vibration modes of the interconnected $[Si(Al)O_4]$ tetrahedra [24,25]. Specifically, the peaks at 425, 550, and 691 cm^{-1} are associated with the symmetric

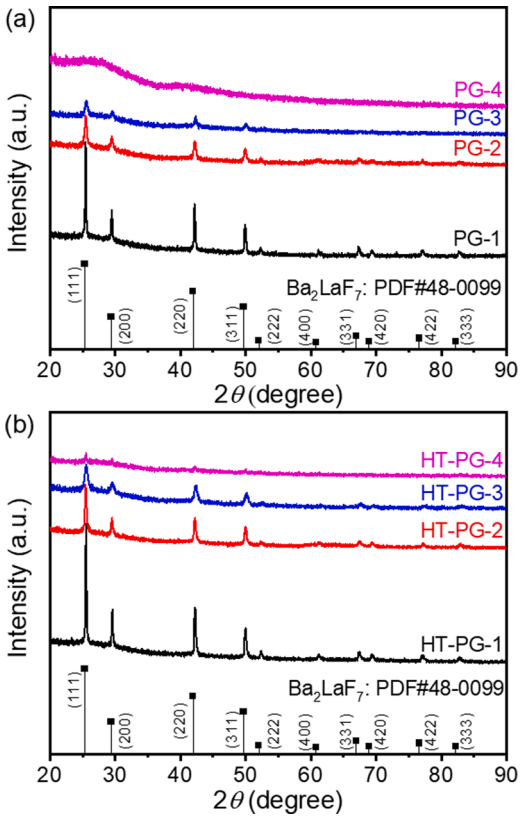

Fig. 3. (a) X-ray diffraction (XRD) patterns of PG-1, PG-2, PG-3, and PG-4 samples, respectively. **(b)** XRD patterns of HT-PG-1, HT-PG-2, HT-PG-3, and HT-PG-4 samples, respectively. Bars represent cubic Ba_2LaF_7 crystal data (PDF#48–0099).

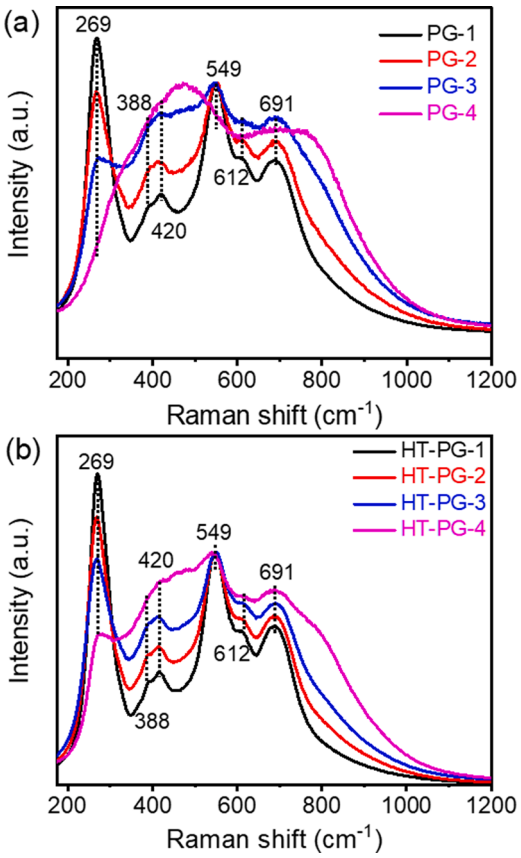

Fig. 4. Normalized Raman spectra of PG **(a)** and the heat-treated PG **(b)** samples, respectively. Note: Raman spectra of PG-4 sample normalized by the maximum intensity; Raman spectra of other samples normalized by the intensity of the peak at around 549 cm^{-1}.

stretch of 5-, 4- and 3-fold rings, respectively [26,27]. Interestingly, only two broad peaks at 474 and 720 cm^{-1} appear in the spectrum of the sample homogenized at 1590 °C (i.e., sample PG-4), indicating the amorphous nature of PG-4 [28]. This implies that the structural heterogeneity in PG samples increases with decreasing T_{homo}, hence promoting formation of Ba_2LaF_7 crystals. In addition, the symmetric stretching vibrational peaks are not detected in PG-4, indicating that the $[Si(Al)O_4]$ tetrahedra are not well interconnected [28].

To investigate the effect of HT on both crystallization and local structure of PG samples, the Raman spectroscopy measurements were conducted on the heat-treated PG samples (Fig. 4b). Compared to the Raman spectra of PG-1, -2 and -3 in Fig. 4a, the Raman peak at 269 cm^{-1} becomes stronger upon HT, indicating an increase of Ba_2LaF_7 crystal content, and this agrees with the XRD evidence (Fig. 3). Moreover, the weak Raman peak at 269 cm^{-1} appears in HT-PG-4 sample, meaning that Ba_2LaF_7 crystals form upon HT. In addition, the Raman peaks related to the symmetric stretching vibration modes of $[Si(Al)O_4]$ tetrahedra also occur in HT-PG-4 sample, which are consistent with those of HT-PG-1, -2 and -3 samples. This indicates that the dissociated glass network containing $[Si(Al)O_4]$ tetrahedra is interconnected again in PG-4 upon HT, being confirmed by the increase of T_g.

Fig. 5 shows the TEM images of samples PG-1, PG-4, HT-PG-1, and HT-PG-4. It is seen in Fig. 5a that flower-like Ba_2LaF_7 crystals are present in the glass matrix of PG-1, and their size increases upon HT. The distance between the adjacent fringes is determined to be 0.35 nm, which matches with the spacing of the (111) planes of Ba_2LaF_7 crystals. Furthermore, new spherical Ba_2LaF_7 nanocrystals emerge in HT-PG-1 sample (Fig. 5c). The TEM image in Fig. 5b confirms the glassy nature of PG-4 sample since there are no distinct lattice fringes. Through HT,

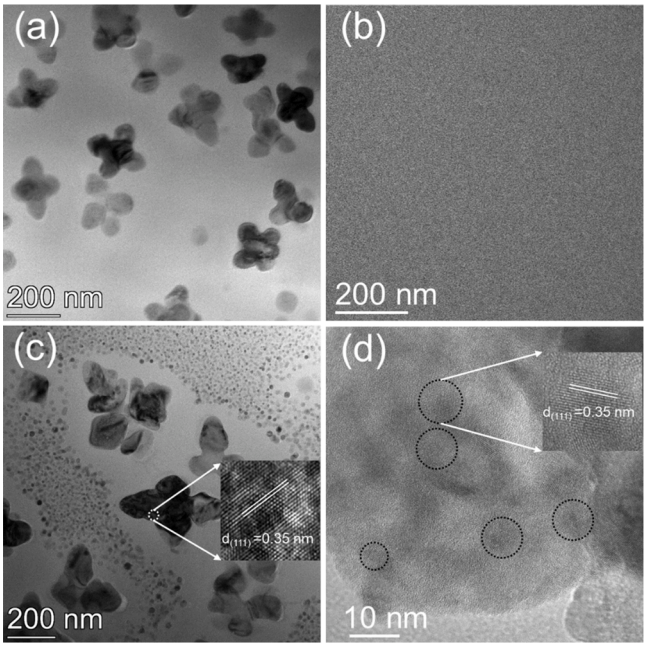

Fig. 5. ACTEM images of PG-1 **(a)**, PG-4 **(b)**, HT-PG-1 **(c)** and HT-PG-4 **(d)** samples, respectively. Note that the flower-like domains (PG-1), small dot regions (HT-PG-1), and regions marked with dashed circles (HT-PG-4) present Ba_2LaF_7 crystals.

some ordered domains of about 10 nm (see the dashed circles) occur in glass matrix and exhibit the spacing of 0.35 nm between the (111) planes (Fig. 5d), indicating the formation of Ba_2LaF_7 crystals (Inset of Fig. 5d).

To study the impact of both T_{homo} and HT on the heterogeneity and crystallization, SEM analyses were performed on samples PG-1, PG-4, HT-PG-1 and HT-PG-4 as shown in Fig. 6. Some flower-like Ba_2LaF_7 crystals of about 200 nm (white domains) are uniformly distributed in PG-1 (Fig. 6a). In contrast, no crystals are detectable in PG-4 (Fig. 6b). This clearly indicates that increasing the homogeneity by elevating

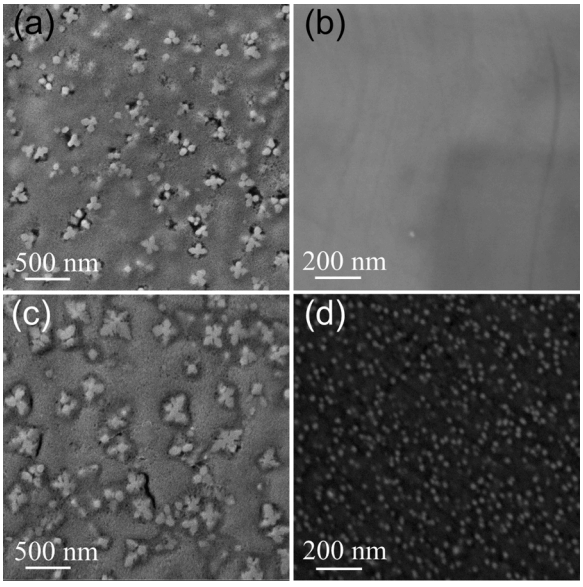

Fig. 6. SEM micrographs of both PG and the heat-treated PG samples, (a) PG-1; (b) PG-4; (C) HT-PG-1; (d) HT-PG-4. For PG-1 and HT-PG-1, white flower-like domains and gray regions are Ba_2LaF_7 crystals and tiny spherical Ba_2LaF_7 nanocrystals, respectively. HT-PG-4, small dot regions are new-formed Ba_2LaF_7 nanocrystals, embedded in the glass matrix (large black areas).

T_{homo} can suppress the formation of Ba_2LaF_7 crystals. In Fig. 6c and d, we can observe the influence of HT on the crystallization behavior of PG samples. For instance, when sample PG-1 is subjected to HT at 643 °C ($1.07T_{c1}$) for 2 hrs, flower-like Ba_2LaF_7 crystals grow up to 300 nm, and at the same time, tiny spherical Ba_2LaF_7 nanocrystals (about 15 nm in size) are precipitated from the glass matrix (see the image of HT-PG-1 in Fig. 6c). When the amorphous sample PG-4 is heat-treated at 642 °C ($1.07T_{c1}$) for 2 hrs, some spherical Ba_2LaF_7 nanocrystals of 10 nm in size are precipitated from the glass matrix of PG-4 sample (Fig. 6d) [29]. This crystallization behavior is also confirmed by the TEM results in Fig. 5.

To reveal the effect of T_{homo} on the microstructures of PG samples, we performed the ^{27}Al magic angle spinning (MAS) nuclear magnetic resonance (NMR) measurements (Fig. 7). It is seen that ^{27}Al MAS NMR spectra of all the samples feature the main resonance at about 60 ppm, which is attributed to the four-coordinated aluminum (Al(IV)) [30]. In addition, the Al(IV) signal in PG-2, -3 and −-4 samples has the same chemical shift as PG-1, suggesting that the coordination environment of Al does not undergo detectable change with increasing T_{homo}. It was previously reported that Al^{3+} ions can be distributed both in the interface regions and in the structural network to form $[Al(O,F)_4]$ and $[Al(O)_4]$ tetrahedra, respectively [31]. However, owing to the volatilization of fluorides (SiF_4 and NaF) and the decrease of the size of fluoride-rich domains with increasing T_{homo}, some Al-F linkages in the interface regions might be replaced by the Al-O linkages. This means that the coordination environment of Al could be slightly altered though this change is not detectable in ^{27}Al NMR spectra.

3.3. Optical properties

Fig. 8a and b show the light transmittance spectra in the range of 275 to 1000 nm of PG and the heat-treated PG samples, respectively. The insets of the figures illustrate the change in transparency of the real samples. The light transmittance (%) spectra are derived from the optical absorption spectra through the equation:

$$Transmittance = 10^{\left(2-\frac{A}{THK}\right)} \quad (1)$$

where A is the absorbance and THK is the sample thickness (in mm). Four main absorption peaks of Er^{3+} ions can be observed at around 378, 486, 521, and 652 nm, which are attributed to the transitions from the ground state $^4I_{15/2}$ to the excited states $^4G_{11/2}$, $^4F_{7/2}$, $^2H_{11/2}$, and $^4F_{9/2}$, respectively [17]. In addition to the above-mentioned peaks, an absorption peak at around 978 nm is seen in each transmittance spectrum,

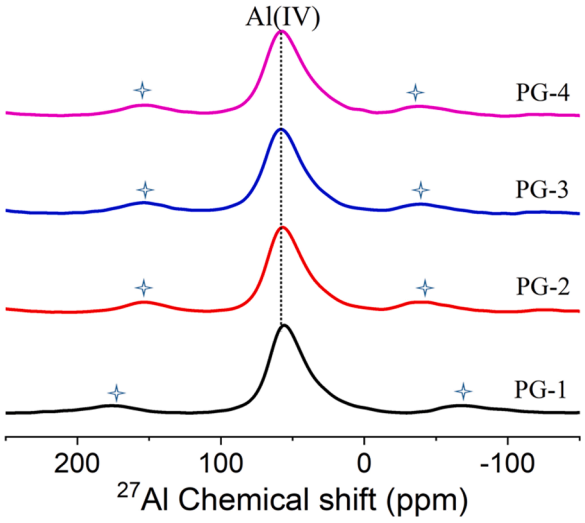

Fig. 7. ^{27}Al magic angle spinning (MAS) NMR spectra of PG-1, PG-2, PG-3, and the PG-4 samples, respectively. (*) denotes spinning sidebands.

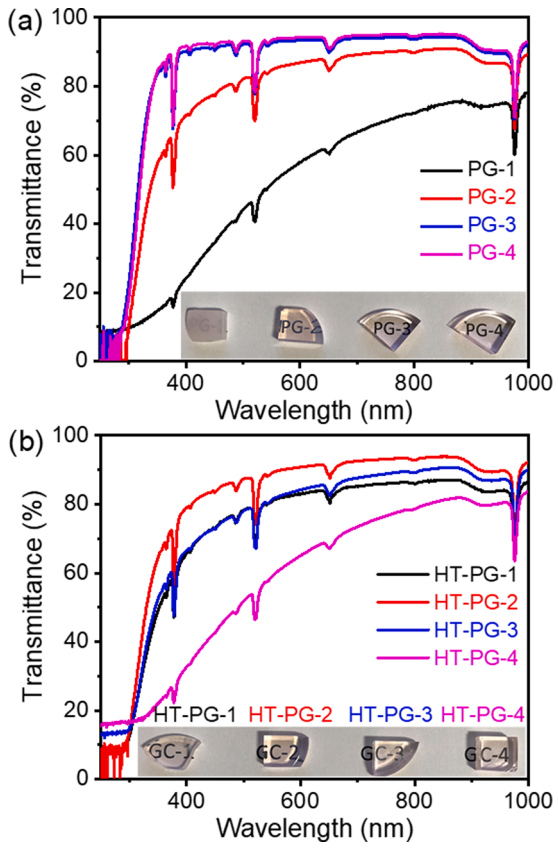

Fig. 8. Light transmittance spectra of PG **(a)** and the heat-treated PG samples **(b)**, respectively. Insets: the optical photographs of the samples (maximum size: about 1 cm).

and it is associated with the transition of Yb^{3+} ions: $^2F_{7/2} \rightarrow {}^2F_{5/2}$. The light transmittance of PG samples increases with increasing T_{homo} (Fig. 8a), reaching the maximum value of around 95% (per mm) in PG-4 sample. This is mainly because raising T_{homo} decreases the size of the Ba_2LaF_7 crystals and alters the chemical composition of the glass matrix. This reduces the differences in the refractive index (n) between the Ba_2LaF_7 crystal (1.54@588 nm) and the remaining glass matrix, thereby suppressing the light scattering and hence leading to the highest light transmittance [32].

Interestingly, the light transmittance of HT-PG-1 and HT-PG-2 samples is even higher than that of samples PG-1 and PG-2 although both the fraction and the size of Ba_2LaF_7 crystals increase upon HT. This anomalous phenomenon is in strong contrast to what is observed in traditional GCs [1]. This means that HT is an effective way to enable the n of glass matrix to match that of Ba_2LaF_7 crystals, and hence to reduce light scattering of the samples [33]. Contrarily, the light transmittance of samples PG-3 and PG-4 is lowered by HT, and therefore the heat-treated PG-3 and PG-4 samples are less transparent than the untreated ones. It was reported that n is proportional to density (ρ) for inorganic glasses [28,34,35]. The ρ values of the 8 studied samples are given in Table 2, demonstrating that ρ is lowered by HT. Thus, it can be inferred that the n value of glass matrix in the heat-treated samples decreases upon HT. Thus, the n differences between Ba_2LaF_7 crystals and the glass matrix for PG-1 and PG-2 become smaller after HT, but PG-3 and PG-4 exhibit the opposite trend.

Table 2
Density (ρ) of PG and the heat-treated PG samples, respectively.

sample	PG-1	PG-2	PG-3	PG-4	HT-PG-1	HT-PG-2	HT-PG-3	HT-PG-4
ρ (g cm^{-3})	3.46	3.47	3.46	3.44	3.45	3.45	3.44	3.42

Fig. 9 shows the UC luminescence spectra in the wavelength range from 500 to 700 nm for the PG and the heat-treated PG samples, which are obtained by excitation of the 980 nm laser. The characteristic UC luminescence peaks at 521, 541, and 652 nm are attributed to the transitions from the excited states: $^2H_{11/2}$, $^4S_{3/2}$, and $^4F_{9/2}$ to the ground state: $^4I_{15/2}$ of Er^{3+} ions, respectively. It is seen that the UC luminescence intensity of PG samples decreases with the increasing T_{homo} (Fig. 9a and its inset) and the heat-treated PG samples exhibit higher UC luminescence intensity than PG samples (Fig. 9b and its inset). In addition, these energy levels in the heat-treated PG samples are more strongly split than PG samples [36]. This behavior in heat-treated samples can be ascribed to the incorporation of more Er^{3+} ions into the low phonon energy environment in Ba_2LaF_7 crystals, reducing the probability of non-radiative relaxation and thus enhancing UC luminescence [37].

By comparing the data in Fig. 8 with those in Fig. 3, we can find an effective way for designing glass-ceramics (GCs) with optimum luminescent behaviors, i.e., regulating both T_{homo} and HT conditions. As described above, the light transparency of PG samples increases with raising T_{homo}, and however, the UC luminescence becomes weaker. Based on these two opposite trends, we can tailor the optical and photonic properties of the GCs, depending on their application fields. If we want to achieve the highest UC luminescence effect (i.e., sample PG-1 in Fig. 9a) in an Er-Yb doped oxyfluoride glass-ceramic, we should fabricate the precursor sample at the lowest T_{homo} (i.e., melting at 1450 °C),

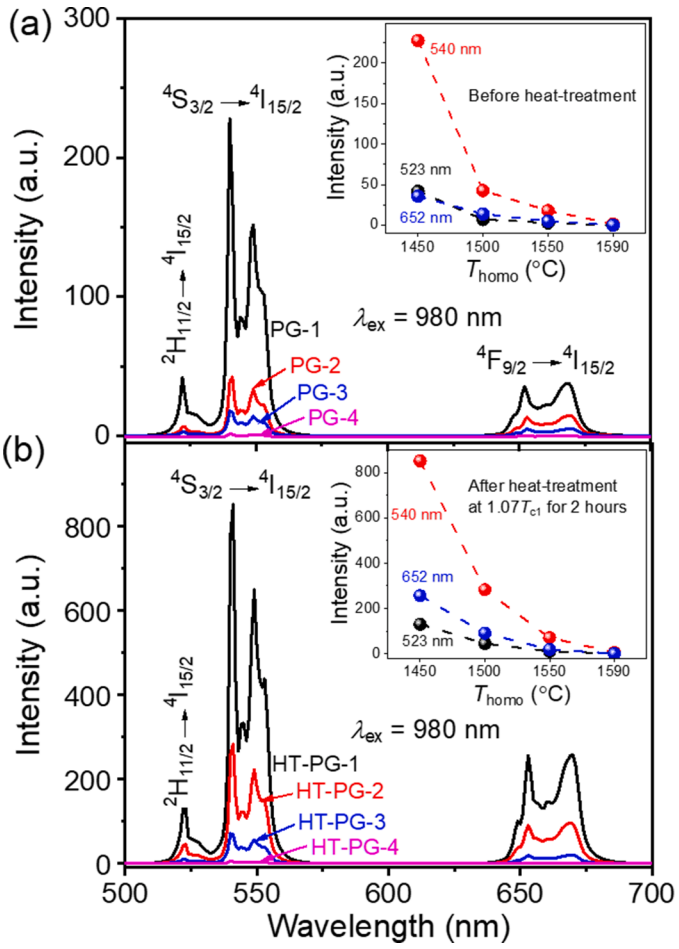

Fig. 9. Up-conversion (UC) luminescence spectra. **(a):** PG samples (PG-1, -2, -3, -4); Inset: the dependence of UC luminescence intensity on T_{homo}. **(b):** The heat-treated PG samples (HT-PG-1, -2, -3, -4); Insets: the dependence of UC luminescence intensity on T_{homo} after HT.

but this sample exhibits the lowest light transmittance (Fig. 8a). However, if we desire to obtain the glass with both high light transmittance (Fig. 8b) and strong UC luminescent effect (Fig. 9b), we can subject it to a proper HT (see sample HT-PG-1). In other words, a proper HT can enable enhancing both light transmittance and UC luminescence. Depending on the application field of such GCs materials, an optimum combination between light transmittance and UC luminescence should be realized by controlling both the T_{homo} and the HT conditions.

4. Conclusion

Four Er^{3+}-Yb^{3+} ions doped oxyfluoride precursor glass (PG) samples were prepared from the sample composition ($45SiO_2$–$15Al_2O_3$–$12Na_2O$-$21BaF_2$–$7LaF_3$–$0.5ErF_3$–$1.0YbF_3$) at four melt-homogenization temperatures (T_{homo}) (1450, 1500, 1550 and 1590 °C), respectively. The effect of T_{homo} on crystallization behavior, structural evolution and optical properties of the studied samples were studied by performing DSC, SEM, XRD, TEM and NMR characterizations and by conducting optical analyses. We found that the crystallization enthalpy (ΔH) corresponding to the first crystallization peak decreases with increasing T_{homo}, indicating a decrease of crystallization tendency in PG samples. This phenomenon could arise from a decrease of the fluoride-rich domains in glass melt, i.e., a decrease in structural heterogeneity. The light transmittance of PG samples increases with increasing T_{homo}. This is attributed to the decrease in both the fraction and the size of Ba_2LaF_7 crystals, and hence, to the lowered difference in the refractive index (n) between the Ba_2LaF_7 crystals and the glass matrix. In addition, the Up-conversion (UC) luminescence of PG samples becomes weaker with increasing T_{homo}. Interestingly, the light transmittance of samples PG-1 and PG-2 samples increased upon heat-treatment (HT), whereas that of PG-3 and PG-4 decreased. Moreover, the heat-treated PG samples exhibit higher crystallinity and stronger UC luminescence than PG samples. Thus, this work provided an effective approach, i.e., the approach optimizing both melt-homogenization temperature and HT conditions, to develop the glass-ceramics with high optical and photonic performances for various applications.

CRediT authorship contribution statement

Zhencai Li: Investigation, Methodology, Data curation, Writing – original draft. **Linling Tan:** Investigation, Writing – original draft. **Chunying Chen:** Data curation. **Dacheng Zhou:** Investigation, Methodology. **Lars R. Jensen:** Investigation, Data curation. **Jinjun Ren:** Data curation, Writing – review & editing. **Yanfei Zhang:** Investigation, Writing – review & editing. **Jianbei Qiu:** Investigation, Methodology, Software, Conceptualization. **Yuanzheng Yue:** Investigation, Supervision, Methodology, Conceptualization, Writing – review & editing.

Declaration of Competing Interest

The authors declare that they have no known competing financial interests or personal relationships that could have appeared to influence the work reported in this paper.

Acknowledgments

This work is supported by the China scholarship council (CSC, No. 201808530502), the National Natural Science Foundation of China (No. 12064021), the Science Foundation of Yunnan Province (202001AT070037), the Taishan Youth Scholar Project of Shandong Province (tsqn202103098) and the Shandong Provincial Natural Science Foundation (ZR2020ME025).

References

[1] X. Liu, J. Zhou, S. Zhou, Y. Yue, J. Qiu, Transparent glass-ceramics functionalized by dispersed crystals, Prog. Mater. Sci. 97 (2018) 38–96.
[2] C.A. Angell, Formation of Glasses from Liquids and Biopolymers, Science 267 (1995) 1924–1935.
[3] C. Bocker, J. Wiemert, C. Rüssel, The formation of strontium fluoride nano crystals from a phase separated silicate glass, J. Eur. Ceram. Soc. 33 (2013) 1737–1745.
[4] K. Sun, D. Tan, X. Fang, X. Xia, D. Lin, J. Song, Y. Lin, Z. Liu, M. Gu, Y. Yue, J. Qiu, Three-dimensional direct lithography of stable perovskite nanocrystals in glass, Science. 375 (2022) 307–310.
[5] S. Bhattacharyya, C. Boeker, T. Heil, J.R. Jinschek, T. Höche, C. Rüssel, H. Kohl, Experimental evidence of self-limited growth of nanocrystals in glass, Nano Lett. 9 (2009) 2493–2496.
[6] J.R. Barros, C. Bocker, C. Rüssel, The effect of Er^{3+} and Sm^{3+} on phase separation and crystallization in $Na_2O/K_2O/BaF_2/BaO/Al_2O_3/SiO_2$ glasses, Solid State Sci. 12 (2010) 2086–2090.
[7] M. Stoica, M. Brehl, C. Bocker, A. Herrmann, C. Rüssel, Microstructure and luminescence of erbiumdoped $Na_2O/K_2O/CaO/CaF_2/Al_2O_3/SiO_2$ nano glass-ceramics, Mater. Chem. Phys. 207 (2018) 36–43.
[8] Z. Zhao, F. Hu, Z. Cao, F. Chi, X. Wei, Y. Chen, C. Duan, M. Yin, Self-crystallized Ba_2LaF_7: Nd^{3+}/Eu^{3+} glass ceramics for optical thermometry, Ceram. Int. 43 (2017) 14951–14955.
[9] W. Shen, Y. Yang, Z. Li, M.I. Khan, E. Cao, D. Zhou, J. Qiu, Effect of melting temperature on the structure of self-crystallized Ba_2LaF_7 glass-ceramics, J. Non. Cryst. Solids 523 (2019), 119579.
[10] D. Chen, Z. Wan, Y. Zhou, P. Huang, Z. Ji, Ce^{3+} dopants-induced spectral conversion from green to red in the Yb/Ho: $NaLuF_4$ self-crystallized nano-glass-ceramics, J. Alloys Compd. 654 (2016) 151–156.
[11] J. Cao, X. Li, Z. Wang, Y. Wei, L. Chen, H. Guo, Optical thermometry based on up-conversion luminescence behavior of self-crystallized K_3YF_6: Er^{3+} glass ceramics, Sens. Actuators, B Chem. 224 (2016) 507–513.
[12] F. Hu, W. Chen, Y. Jiang, W. Song, R. Wei, H. Guo, Tm^{3+}-doped $Na_{0.5-x}Yb_{0.5+x}F_{2+2x}$ self-crystallization glass ceramics: Microstructure and optical thermometry properties, J. Lumin. 214 (2019) 0–4.
[13] X. Xu, W. Zhang, D. Yang, W. Lu, J. Qiu, S.F. Yu, Phonon-Assisted Population Inversion in Lanthanide-Doped Upconversion Ba_2LaF_7 Nanocrystals in Glass-Ceramics, Adv. Mater. 28 (2016) 8045–8050.
[14] Y. Yue, Revealing the nature of glass by the hyperquenching-annealing-calorimetry approach, J. Non. Cryst. Solids X. 14 (2022), 100099.
[15] Y. Yue, Experimental evidence for the existence of an ordered structure in a silicate liquid above its liquidus temperature, J. Non. Cryst. Solids 345-346 (2004) 523–527.
[16] N. Lonnroth, Y. Yue, Structural order and crystallization of an iron-rich aluminosilicate liquid under oxidizing condition, J. Non. Cryst. Solids 354 (2008) 1190–1193.
[17] Z. Li, D. Zhou, L.R. Jensen, J. Qiu, Y. Zhang, Y. Yue, Er^{3+}-Yb^{3+} ions doped fluoro-aluminosilicate glass-ceramics as a temperature-sensing material, J. Am. Ceram. Soc. 104 (2021) 4471–4478.
[18] Q. Zheng, Y. Zhang, M. Montazerian, O. Gulbiten, J.C. Mauro, E.D. Zanotto, Y. Yue, Understanding Glass through Differential Scanning Calorimetry, Chem. Rev. 119 (2019) 7848–7939.
[19] H. Liu, A. Qiao, Y. Gao, H. Tao, X. Zhao, Y. Hu, Y. Yue, Reversible formation-melting of nano-crystals in supercooled oxyfluoride germanate liquids, J. Eur. Ceram. Soc. 39 (2019) 5373–5379.
[20] S. Liu, Y. Kong, H. Tao, Y. Sang, Crystallization of a highly viscous multicomponent silicate glass: Rigidity percolation and evidence of structural heterogeneity, J. Eur. Ceram. Soc. 37 (2017) 715–720.
[21] C. Lin, C. Bocker, C. Rüssel, Nanocrystallization in Oxyfluoride Glasses Controlled by Amorphous Phase Separation, Nano Lett. 15 (2015) 6764–6769.
[22] S. Zhao, S. Xu, D. Deng, X. Fan, Intense upconversion luminescence of Er^{3+}/Yb^{3+} codoped oxyfluoride borosilicate glass ceramics containing Ba_2GdF_7 nanocrystals, J. Rare Earths 28 (2010) 903–906.
[23] J. Zhao, X. Xu, P. Li, X. Li, D. Chen, X. Qiao, J. Du, G. Qian, X. Fan, Structural Origins of $RF_3/NaRF_4$ Nanocrystal Precipitation from Phase-Separated SiO_2-Al_2O_3-RF_3-NaF Glasses: A Molecular Dynamics Simulation Study, J. Phys. Chem. B 123 (2019) 3024–3032.
[24] X. Fan, J. Wang, X. Qiao, M. Wang, J.L. Adam, X. Zhang, Preparation process and upconversion luminescence of Er^{3+}-doped glass ceramics containing Ba_2LaF_7 nanocrystals, J. Phys. Chem. B 110 (2006) 5950–5954.
[25] Y. Peng, J. Zhong, X. Li, J. Chen, J. Zhao, X. Qiao, D. Chen, Controllable competitive nanocrystallization of La^{3+}-based fluorides in aluminosilicate glasses and optical spectroscopy, J. Eur. Ceram. Soc. 39 (2019) 1420–1427.
[26] H. Aguiar, J. Serra, P. González, B. León, Structural study of sol-gel silicate glasses by IR and Raman spectroscopies, J. Non. Cryst. Solids 355 (2009) 475–480.
[27] Q. Liu, Y. Tian, C. Wang, F. Huang, X. Jing, J. Zhang, X. Zhang, S. Xu, Different dominant transitions in holmium and ytterbium codoped oxyfluoride glass and glass ceramics originating from varying phonon energy environments, Phys. Chem. Chem. Phys. 19 (2017) 29833–29839.
[28] S. Kang, Z. Huang, W. Lin, D. Yang, J. Zhao, X. Qiao, X. Xiao, S. Xu, J. Qiu, J. Du, G. Dong, Enhanced single-mode fiber laser emission by nano-crystallization of oxyfluoride glass-ceramic cores, J. Mater. Chem. C 7 (2019) 5155–5162.
[29] A. Astruc, S. Célérier, E. Pavon, A.S. Mamede, L. Delevoye, S. Brunet, Mixed $Ba_{1-x}La_xF_{2+x}$ fluoride materials as catalyst for the gas phase fluorination of 2-chloropyridine by HF, Appl. Catal. B Environ. 204 (2017) 107–118.

[30] T. Zhao, L. Hu, J. Ren, Fluorophosphate Upconversion-Luminescent Glass-Ceramics Containing Ba_2LaF_7: Er^{3+} Nanocrystals: An Advanced Solid-State Nuclear Magnetic Resonance Study, J. Phys. Chem. C 125 (2021) 26901–26915.
[31] J. Zhao, R. Ma, X. Chen, B. Kang, X. Qiao, J. Du, X. Fan, U. Ross, C. Roiland, A. Lotnyk, L. Kienle, X. Zhang, From Phase Separation to Nanocrystallization in Fluorosilicate Glasses: Structural Design of Highly Luminescent Glass-Ceramics, J. Phys. Chem. C 120 (2016) 17726–17732.
[32] T. Berthier, V.M. Fokin, E.D. Zanotto, New large grain, highly crystalline, transparent glass-ceramics, J. Non. Cryst. Solids 354 (2008) 1721–1730.
[33] Z. Li, C. Chen, W. Shen, D. Zhou, L.R. Jensen, X. Qiao, J. Ren, J. Du, Y. Zhang, J. Qiu, Y. Yue, Transformation from Translucent into Transparent Rare Earth Ions Doped Oxyfluoride Glass-Ceramics with Enhanced Luminescence, Adv. Opt. Mater. (2022), 2102713.
[34] H.N. Ritland, Relation Between Refractive Index and Density of a Glass at Constant Temperature, J. Am. Ceram. Soc. 38 (1955) 86–88.
[35] Y.Y. Huang, A. Sarkar, P.C. Schultz, Relationship between composition, density and refractive index for germania silica glasses, J. Non. Cryst. Solids 27 (1978) 29–37.
[36] J. Qiu, Q. Jiao, D. Zhou, Z. Yang, Recent progress on upconversion luminescence enhancement in rare-earth doped transparent glass-ceramics, J. Rare Earths 34 (2016) 341–367.
[37] J. Cai, X. Wei, F. Hu, Z. Cao, L. Zhao, Y. Chen, C. Duan, M. Yin, Up-conversion luminescence and optical thermometry properties of transparent glass ceramics containing CaF_2:Yb^{3+}/Er^{3+} nanocrystals, Ceram. Int. 42 (2016) 13990–13995.